Geochemical diversity of continental arc basaltic mushy reservoirs driven by reactive melt infiltration

Check for updates

Jun-Yong Li[1], Xiao-Lei Wang [1]✉, Zhi-Dong Gu[2], Di Wang[1] & De-Hong Du[1]

The reactive melt flow emerges as an important factor for diversification of basaltic magmatic reservoirs, but whether and how it influences continental arc basaltic mushes are enigmatic. Here, we used mineral and whole-rock geochemistry to examine the petrogenesis of a suit of mafic and intermediate plutons in western Yangtze Block, which were emplaced at continental arc crust and primarily had plagioclase and clinopyroxene as early cumulate mineral phases. We found the crystal mushes were infiltrated by externally-derived reactive melt with high $\delta^{18}O$ and fertile crustal signatures, resulting in the changes of mineral phases (e.g., clinopyroxene transformed to hornblende) and bulk-rock geochemistry (including isotopes). Then, the reacted granitic melt was prone to either be extracted from or stall in the crystal mushes, generating quartz-poor (mafic) or quartz-rich (intermediate) plutons, respectively. This study supports the reactive melt infiltration may serve as an important engine for compositional diversity of basaltic mush system within continental arc settings.

Incremental mantle-derived melts added into the crust contribute to the formation of transcrustal basaltic magmatic reservoirs and crustal growth and reworking. However, how the basaltic magmatic reservoirs differentiate within the crust is controversial[1–4]. In classic melt-dominated magma chamber paradigm, the differentiation is suggested to be primarily controlled by slow removal of crystals along walls of chamber (i.e., fractional crystallization)[5,6]. Recently, it has been shown that differentiation is generally correlated to crystal-melt separation in crystal-dominated mush through compaction, convective or diffusive exchange, gas-driven filter pressing, or Darcy flow[7–11]. Besides, the complicated open crystal-mush system could also interact with the reactive melt flow[3,12–17]. This mechanism involves a network of melt percolating through a porous crystal framework and reacting with the surrounding crystals, resulting in dissolution-reprecipitation process of the minerals and consequent bulk geochemical modulation. On the other hand, the reactive melt flow is generally accompanied with mush compaction and associated melt extraction, which could further complicate geochemistry of the crystal mush. As a result, the reactive melt flow emerges as a prominent factor differentiating basaltic mushy reservoirs. Its influence was firstly revealed in continental layered intrusions[12,18–20], and then developed in the oceanic gabbroic cumulates in different tectonic settings (i.e., fossil mid-ocean ridge[15,21,22], oceanic island[23], and island arc[14]). Continental arcs witness extensive juvenile magmatism and could serve as ideal sites to investigate the differentiation processes of

continental basaltic mushy system[24]. Their magma differentiation is generally interpreted to involve complex interplay between crystal fractionation, assimilation, and magma mixing[24]. However, whether the reactive melt infiltration was operative and how it influences the magma reservoirs are enigmatic.

Here, by examining the petrogenesis of a suit of mafic and intermediate plutons from a Neoproterozoic deep arc section in western Yangtze Block of South China, we found the interconnected reactive melt (±hornblende-equilibrium melt extraction) considerably modified early-crystallized mineral phases and bulk-rock compositions, and it can serve as an important mechanism controlling compositional diversity of continental arc magmas.

Results
Geological context and petrography
The Yangtze Block is located in the northwestern part of the South China Block and is bounded with the Cathaysia Block to the southeast by the Jiangnan Orogen. It records remarkable crustal growth and reworking during Neoproterozoic, with the western margin characterized by prolonged continental arc magmatism in the period of ca. 860 Ma to ca. 750 Ma[25–27] (Fig. 1a). Miocene extrusion and thrust processes[28] gave rise to well-exposed Neoproterozoic deep arc sections and linearly distributed igneous rocks spanning over 800 km (Fig. 1c). The Neoproterozoic Pengguan Complex (PC) is the

[1]State Key Laboratory for Mineral Deposits Research, School of Earth Sciences and Engineering, Frontiers Science Center for Critical Earth Material Cycling, Nanjing University, Nanjing, China. [2]Research Institute of Petroleum Exploration and Development, PetroChina, Beijing, China. ✉e-mail: wxl@nju.edu.cn
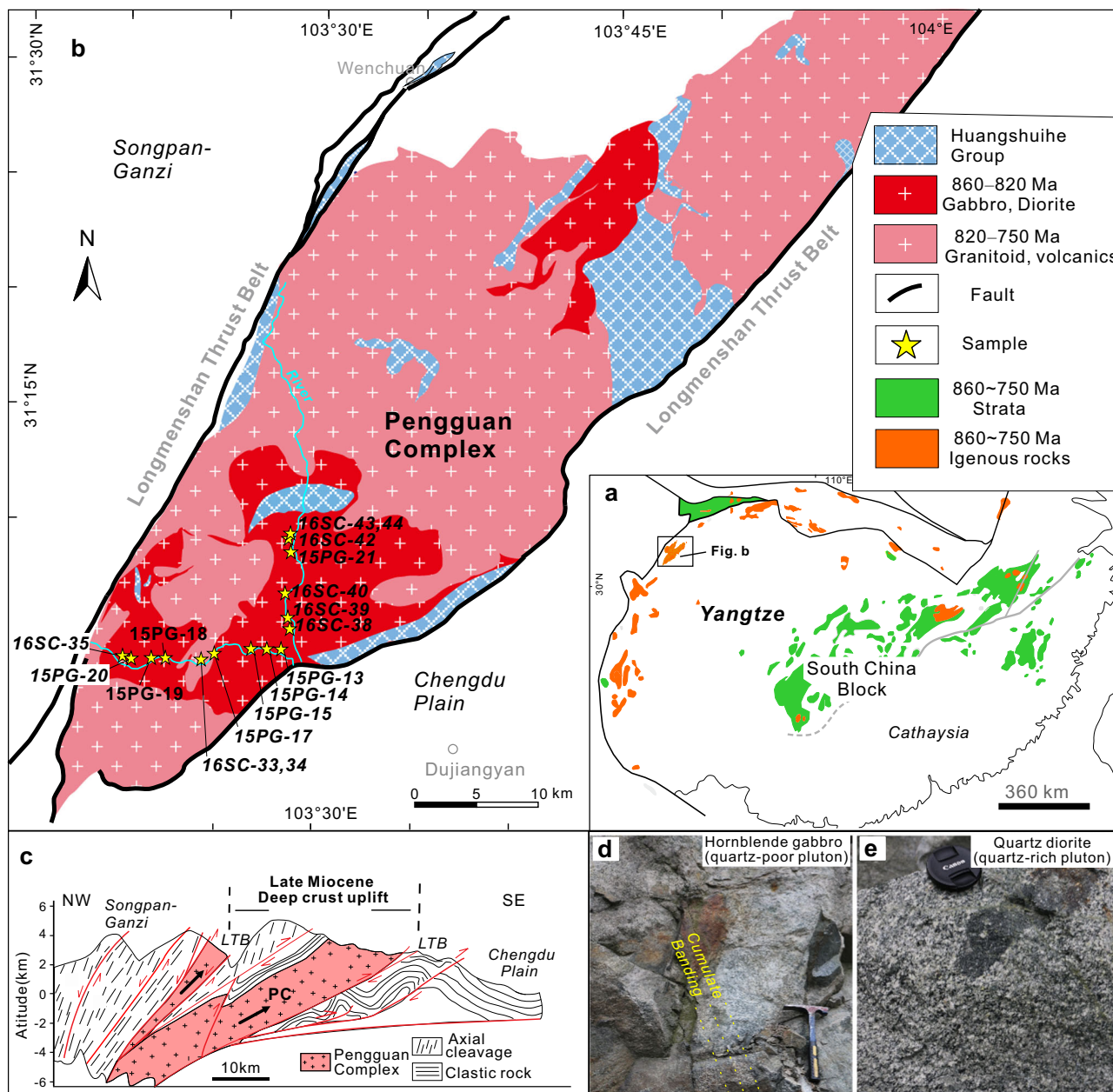
Fig. 1 | Geological background and field photos of the Pengguan Complex (PC).
a Simplified geologic map showing widespread 860–750 Ma strata and igneous rocks in the Yangtze Block, which were linked to ocean-continent subduction process.
b Geological map of the PC and sample locations. The PC represents part of fossil Neoproterozoic continental arc section along the western Yangtze Block. **c** Cross section showing the uplift of the PC during the Late Miocene deformation process (after Wang and Meng[28]). LTB Longmenshan Thrust Belt. **d–e** Representative field photos of quartz-poor and quartz-rich plutons within the PC. The cumulate banding can be seen in the quartz-poor pluton.

largest plutonic mid- to upper-crustal basement unit exposed in the area[29] (Fig. 1b). Our research focused on samples collected from the central region of the PC, comprising of hornblende gabbro, diorite, quartz diorite, and granodiorite (dark red areas in Fig. 1b).

These samples predominantly exhibit cumulate textures and have similar mineral assemblages, with main mineral phases of plagioclase (Pl), clinopyroxene (Cpx), hornblende (Hbl), actinolite (Act), quartz (Qz), and chlorite (Chl), albeit with varying proportions (Figs. 2–3, Supplementary Fig. 1; and Supplementary Table 1). Minor proportions (<1 vol%) of apatite, zircon, magnetite, ilmenite, biotite, (±) orthopyroxene, (±) orthoclase, (±) sphere are also present. The plagioclase grains are subhedral–euhedral and may represent earlier cumulate phases. They were partially altered to sericite and albite, with some of them exhibiting albite rims (e.g., sample 15PG-13-3 in

Supplementary Fig. 1) that possibly indicative of mineral-melt interaction. The hornblende (Hbl) has an irregular morphology. It is closely associated with clinopyroxene and sometimes replaces clinopyroxene along its rims or cleavage planes, leaving the clinopyroxene residues with irregular morphologies (Fig. 2c–f and Supplementary Fig. 2). This suggests that the formation of hornblende may occur at the expense of clinopyroxene precursors through peritectic reactions[14,30], rather through equilibrium crystallization processes. The Cpx-Hbl association generally exhibits subhedral shapes, partially corroded or fragmented textures, and often displays a poikilitic texture in most samples. This implies that the clinopyroxene likely crystallized after plagioclase, followed by the formation of peritectic hornblende. Quartz in the samples typically contacts with hornblende, coexists with zircon, and serves as an interstitial
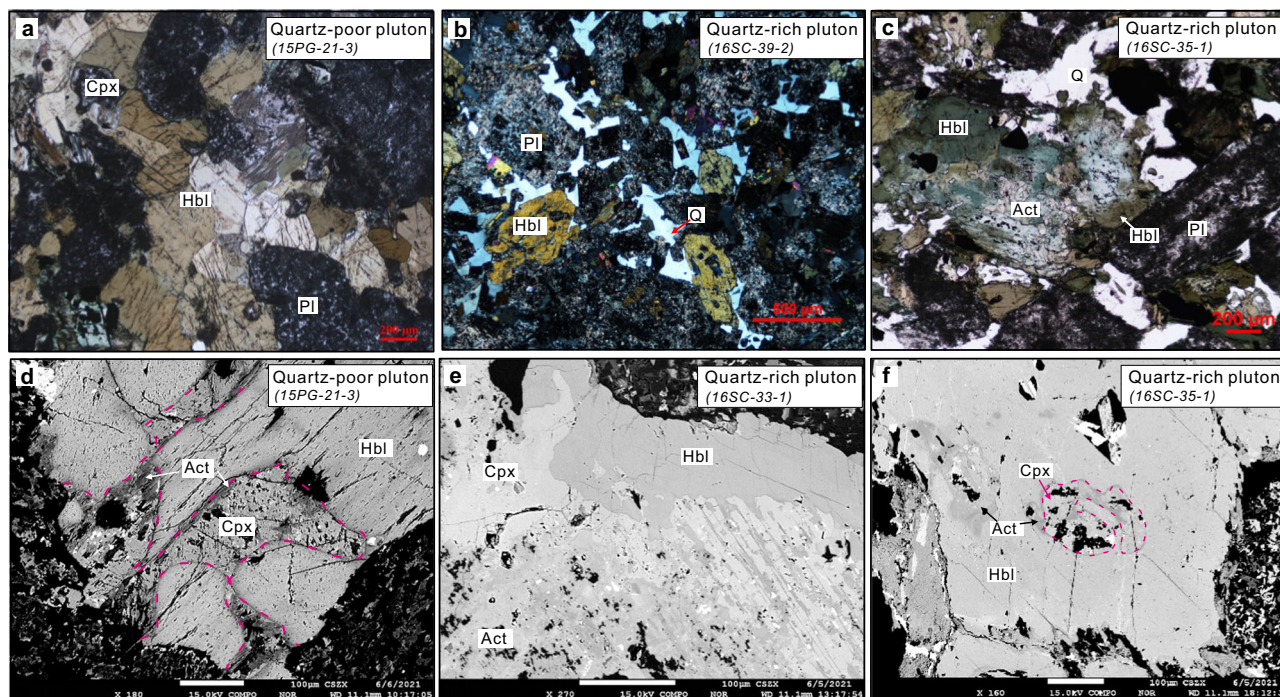
Fig. 2 | Micrographs of typical quartz-poor and quartz-rich samples in the PG.
a A quartz-poor pluton typically consists of clinopyroxene, hornblende and plagi-
oclase. The plagioclase was extensively replaced by albite and mica. **b** A quartz-rich
pluton typically consists of cumulate hornblende and plagioclase, with quartz
occurring as an anhedral interstitial phase. **c** The actinolite is surrounded by
hornblende in a quartz-rich sample. **d–f** Both plutonic types preserve the
clinopyroxene-hornblende replacement texture as shown in backscattered electron
(BSE) images. Hbl hornblende, Cpx clinopyroxene, Act actinolite, Pl plagioclase,
Q quartz.

phase filling within the earlier-crystalized mineral skeleton (Supple-
mentary Figs. 5–6). The actinolite is observed to develop along
cleavage planes and grain boundaries of clinopyroxene and horn-
blende (Fig. 2c–f and Supplementary Fig. 2), and the chlorite gen-
erally develops along the rims of biotite (Supplementary Fig. 5). Their
formation in samples were interpreted to be resulted from later
hydrothermal alteration.

Sample classification, mineral, and bulk-rock compositions
We divided the plutonic samples into two types based on their quartz
contents: quartz-poor (<5 vol% quartz; hornblende gabbro and
diorite) and quartz-rich (≥5 vol% quartz; quartz diorite and grano-
diorite) rocks, represented by samples 15PG-21-3 and 16SC-33-1
respectively (Figs. 2–3). The two types exhibit notable distinctions
in terms of petrographic texture, as well as bulk and mineral
compositions. The quartz-poor pluton demonstrates a strong
preferred orientation of plagioclase (e.g., alignment factor of 0.46 in
Fig. 3b), in contrast to the quartz-rich pluton, which exhibits a weak
preferred orientation of plagioclase (e.g., alignment factor of 0.06
in Fig. 3a).

In relation to major elements, the quartz-poor samples are mafic in
composition (SiO_2 = 43–51 wt%), different from the intermediate com-
position of quartz-rich samples (SiO_2 = 50–68 wt%) (Fig. 4). The quartz-
poor samples generally exhibit higher contents of FeO^T (9–16 wt%),
MgO (3.2–6.9 wt%), TiO_2 (1.0–3.6 wt%), CaO (7–11 wt%), and P_2O_5
(0.2–1.7 wt%), but lower contents of K_2O (0.5–1.2 wt%) compared to the
quartz-rich samples (FeO^T = 4–11 wt%; MgO = 0.6–3.7 wt%; TiO_2 =
0.5–1.2 wt%; CaO = 4–7 wt%; P_2O_5 = 0.1–0.3 wt%; K_2O = 1.2–2.4 wt%)
(Supplementary Data 1). Regarding trace elements normalized to
chondrite or primitive mantle (Fig. 5c–d), the two plutonic types show
similar geochemical features in some aspects, such as enrichments of
large-ion lithophile (LILE) and light rare-earth elements (LREE), positive
Pb and K, and negative Nb anomalies. However, the quartz-poor samples
generally have higher concentrations of compatible elements (such as Sc,

V, Cr, Co, Cu), but lower concentrations of incompatible elements (such
as Rb, Pb, La, Th, U, Zr, Hf) compared to the quartz-rich samples (Fig. 5).
Several quartz-poor samples show positive Eu and P anomalies
(Fig. 5c–d), indicating potential accumulation of plagioclase and apatite
in these samples. The wide ranges of bulk-rock MgO (0.6–6.9 wt%) and
compatible elements, such as V (19–363 ppm), Co (2.2–42 ppm), and Sc
(2.6–82 ppm), in all samples are interpreted as a result of varying pro-
portions of mafic mineral accumulation.

The plagioclase grains in quartz-poor samples are anorthite
(An)-richer (51–59) than those (An=44–49) in quartz-rich samples
(Supplementary Data 2). The clinopyroxene in both categories
straddles the augite-diopside compositions (Fig. 6a), while the clin-
opyroxene grains of quartz-poor pluton have slightly higher $Mg^\#$
[71.3–74.9; $Mg^\#$=100*Mg/(Mg+Fe) in mole] than those (65.6–70.5)
of quartz-rich pluton. The actinolite in both categories are MgO-rich,
shows wide range of $Mg^\#$ (~55–73), and exhibits intermediate com-
positions of major elements between clinopyroxene and hornblende
(Fig. 4). The hornblende in quartz-poor samples is predominantly
tschermakite (Fig. 6b) and has higher Al_2O_3 contents (9.2–11.7 wt%),
$Mg^\#$ (55–72), and $(Na+K)_A$ contents (~0.2–0.6 a.p.f.u). In contrast,
the hornblende in quartz-rich samples is magnesio-hornblende with
lower Al_2O_3 contents (4.6–10.0 wt%), $Mg^\#$ (39–65), and $(Na+K)_A$
contents (~0.0–0.4 a.p.f.u; Supplementary Data 2).

Both clinopyroxene and hornblende exhibit notable variations in the
concentrations of incompatible trace elements (Fig. 6c–f and Supplemen-
tary Data 3). Generally, the concentrations of trace elements tend to be
higher in hornblende compared to clinopyroxene, with the exception of Li,
Th, U and Pb. In chondrite-normalized REE diagrams (Fig. 6c, d), clin-
opyroxene displays pronounced negative Eu anomalies (Eu/Eu* =
0.44–0.75, chondrite normalized $Eu/\sqrt{Sm*Gd}$), depletion in La relative to
Sm $[(La/Sm)_N = 0.26–0.97]$, and slight MREE/HREE enrichment $[(Sm/
Yb)_N = 1.31–2.41]$. The hornblende exhibits weak to positive Eu anomalies,
ranging from 0.61 to 1.29. It also demonstrates depletion in La relative to
Sm $[(La/Sm)_N = 0.65–1.05]$, and slight MREE/HREE enrichment
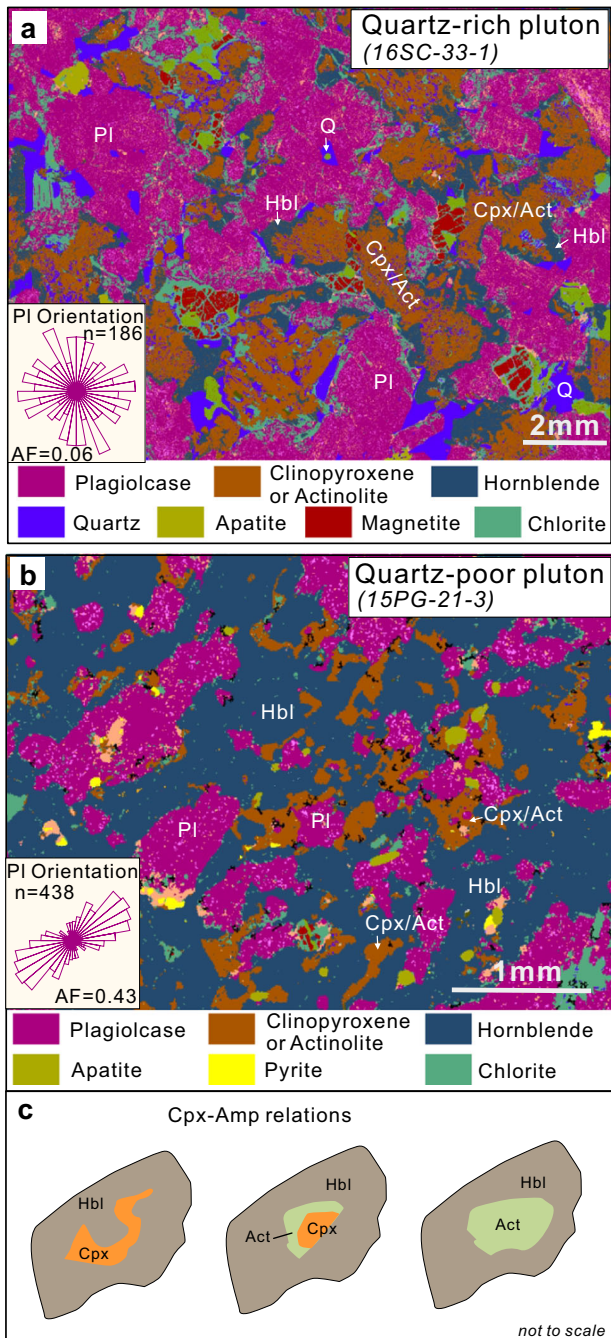
Fig. 3 | Mineral phase mapping and cartoons of typical Cpx-Amp relations.
a, b TIMA (Tescan Integrated Mineral Analyzer) mapping images (in part) for typical quartz-poor and quartz-rich plutons. The rose diagrams on the lower left show the plagioclase orientation of the long axis of the ellipsoid fitted to each grain using the Image J and CSD (Crystal Size Distribution) corrections programs[47].
c Cartoons illustrating three representative Cpx-Amp relations observed in studied samples. Hbl hornblende, Cpx clinopyroxene, Act actinolite, Pl plagioclase, Q quartz.

$[(Sm/Yb)_N = 1.89–3.00]$. In primitive mantle normalized diagrams (Fig. 6e–f), the clinopyroxene shows slight enrichments of Li, Pb, Th, U and REEs, as well as negative peaks of high field strength elements (HFSEs; Zr, Hf, Nb, Ta) and LILEs (Ba, Sr). The transitional metals are either less enriched (i.e., Sc, V, and Zn) or depleted (i.e., Co). Principally, the REE and trace element profiles of hornblende closely resemble those of associated clinopyroxene within the same sample (Fig. 6c–f), with the exception that hornblende exhibits notable enrichments in Rb, Ba, Nb, Ta, Th, and U and

slight depletion in Li, indicating the possible formation of hornblende through breakdown of clinopyroxene via a peritectic reaction.

Bulk-rock and mineral isotopes

All zircon grains show weak CL intensity, and display broad oscillatory zoning without alteration rims (Supplementary Fig. 3). Zircon U-Pb dating results for eight samples indicate that they formed synchronously at ca. 840–820 Ma within uncertainties (Supplementary Fig. 3). Overall, all zircon Hf–O isotope analyses show variable $\varepsilon_{Hf}(t)$ values from –0.7 to +13.5 ($n = 54$) and $\delta^{18}O$ values of 6.05–7.40‰ ($n = 55$), indicative of a predominantly juvenile origin with the addition of ancient supracrustal material (Fig. 7a and Supplementary Data 4). Zircon grains from quartz-rich samples show more variable $\varepsilon_{Hf}(t)$ and $\delta^{18}O$ values compared to those from quartz-poor samples (Fig. 7a). Moreover, the bulk-rock Nd ($\varepsilon_{Nd}(t)$ primarily ranging from –4.0 to 0) and Sr isotopes $[(^{87}Sr/^{86}Sr)_i = 0.7049–0.7085]$ of samples generally exhibit enriched signatures that are decoupled from the zircon Hf isotopes (Fig. 7b and Supplementary Data 1).

The quartz grains in samples 15PG-15-2, 15PG-18-2, and 15PG-21-6 are irregular in shape and exhibit dark and homogeneous (or slightly mottled) luminescent intensity (Fig. 7c). These CL characteristics indicate that quartz either initially precipitated without any discernible CL texture under stable conditions of high temperature and pressure, or that a pre-existing CL-texture was subdued by annealing under metamorphic conditions[31]. The $\delta^{18}O$ values of quartz in each sample are homogeneous, ranging from 9.52 to 10.7‰ for 15PG-15-2 ($n = 14$), 9.76 to 10.6‰ for 15PG-18-2 ($n = 15$) and 11.6–12.9‰ for 15PG-21-6 ($n = 14$), with the average $\delta^{18}O$ values of 10.1 ± 0.7‰ (2 SD), 10.1 ± 0.4‰ (2 SD) and 12.2 ± 0.9‰ (2 SD), respectively (Supplementary Fig. 4 and Data 5). The average $\delta^{18}O$ values of quartz are approximately 3.6‰ to 5.0‰ higher than those of magmatic zircon in the same sample (Fig. 7c).

Discussion
Open-system differentiation with presence of externally-derived melts

The samples in this study exhibit cumulate textures, with euhedral–subhedral plagioclase (An = 44–59) and clinopyroxene ($Mg^\# = 65.6–74.9$) serving as earlier crystallization minerals and constituting the primary silicate crystal frameworks. Subsequently, the clinopyroxene was partially replaced by anhedral hornblende (Fig. 3c). And the mineral mapping results show that the volume ratios between (Cpx+Act) and Hbl are approximately 1:7 for the representative quartz-poor pluton 15PG-21-3 and about 3:2 for representative quartz-rich pluton 16SC-33-1 (Supplementary Table 1). The hornblende likely formed at high temperatures, given the obtained temperatures of ca. 790–850 °C from machine-leaning-based Hbl-thermometry[32] and of ca. 600–875 °C (mostly within range of 710–870 °C) from Ti-in-amphibole thermometer[33] (Supplementary Data 2). Therefore, the replacement of clinopyroxene by hornblende is likely to occur during late magmatic stage with temperature exceeding 700 °C. On the other hand, the Cpx-Hbl replacement, associated with peritectic reaction between clinopyroxene and evolved hydrous melt, could provide insights into whether magmatic differentiation took place in an open or closed system[14,30]. A closed-system differentiation requires the evolved melt was solely the magma residual melt, whereas the evolved melt for open-system differentiation was involved in externally-derived melt. Zircon in hydrous parental basalts generally saturates and crystallizes at late magmatic stage when residual melt evolves to $SiO_2 > 65$ wt% at temperature of ~850–750 °C[34]. We hence could employ the zircon, along with quartz, which crystallized during late magmatic stage and coexisted in our samples (Supplementary Figs. 5–6), to trace the influence of external melts.

The oxygen isotopic compositions of quartz in each sample are homogeneous, with the variations of $\delta^{18}O$ values less than 1.3 ‰.
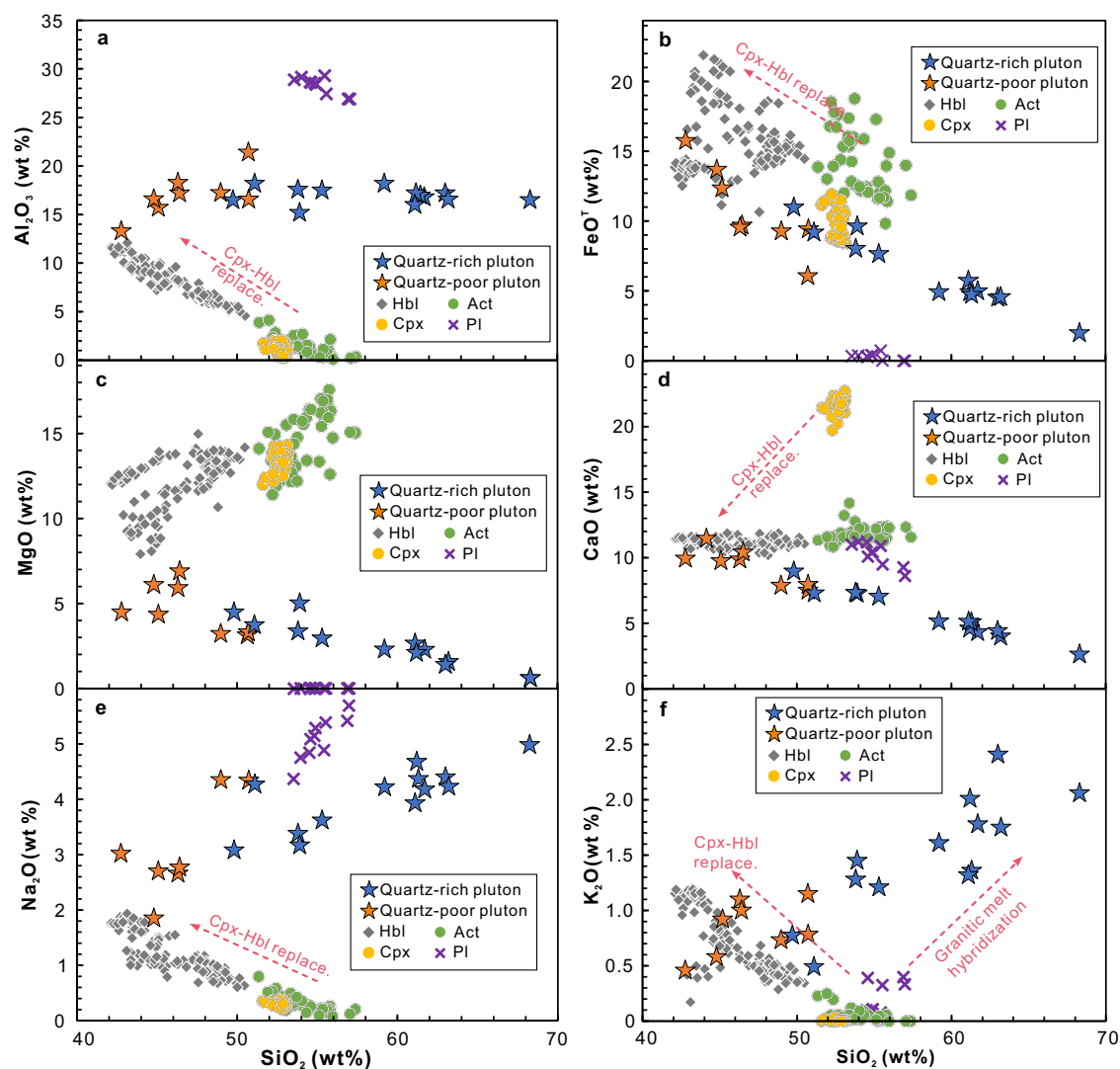
Fig. 4 | Variation of whole-rock major elements to distinguish the quartz-rich pluton from the quartz-poor pluton. a–f Measured compositions of plagioclase, hornblende, actinolite, and clinopyroxene are also shown. Tendency of bulk-rock compositional variation induced by Cpx-Hbl replacement or granitic melt hybridization is shown in the diagrams. The granitic melt is thought to be in equilibrium with the hornblende and shows different fates in quartz-poor and quartz-rich samples (see discussion). Hbl hornblende, Cpx clinopyroxene, Act actinolite, Pl plagioclase.

This indicates the quartz crystallized uniformly and was unlikely to have been altered by hydrothermal fluid flow[35]. Besides, the absence of observable fluid conduits in quartz CL images and alteration rim in the zircon CL images (Supplementary Figs. 3–4) discounts the involvement of fluids that may have affected the oxygen composition of quartz. According to the oxygen-isotope fractionation diagram (Fig. 7c), the high $\delta^{18}O$ values of quartz are not equilibrated with zircon $\delta^{18}O$ at temperatures above 700 °C, which is inconsistent with a closed-system magmatic differentiation. Instead, the elevated $\delta^{18}O$ of the quartz could be explained by introduction of external high-$\delta^{18}O$ silicate melts during the late magmatic stage. Additionally, the negative correlation between zircon $\delta^{18}O$ and $\varepsilon_{Hf}(t)$ values, as well as the decoupling between bulk-rock Nd and zircon Hf isotopic signatures (Fig. 7a–b), further supports the potential involvement of external melts with high $\delta^{18}O$ and enriched Hf and Nd isotopes during late magmatic differentiation. Mineral chemistry also supports an open-system differentiation. It's noteworthy that all analyzed clinopyroxene domains exhibit pronounced negative Eu/Eu* anomalies, while the analyzed hornblende domains display weak to positive Eu/Eu* anomalies (Fig. 6c, d). This indicates that the two mineral types crystallized from plagioclase-saturated and plagioclase-

undersaturated melts, respectively, possibly implying an infiltration of more water-rich and oxidizing melts during the peritectic reaction to form hornblende[14].

The above lines of evidence suggest the studied basaltic mushy reservoirs may have differentiated within an open system, characterized by the involvement of externally derived melts that were potentially high-$\delta^{18}O$ and derived from ancient crustal materials. The external melts possibly mixed with residual magma melts. Their mixture was expected to be chemically reactive and likely formed an interconnected network along grain boundaries, facilitating pervasive chemical exchange with matrix crystals (i.e., clinopyroxene and plagioclase).

Geochemical change of basaltic mush induced by reactive melt infiltration

An interconnected melt network along grain boundaries within mush reservoirs could be easily achieved when the melt proportion is above a threshold value (typically <2%) to permit melt migration through the crystal mush[13,36]. This allows the ingress of externally-derived melts into the migrated melt network, and pervasively chemical reaction between reactive melts and matrix crystals. In this study, both quartz-poor and quartz-rich plutons witnessed the infiltration of externally-derived melts.
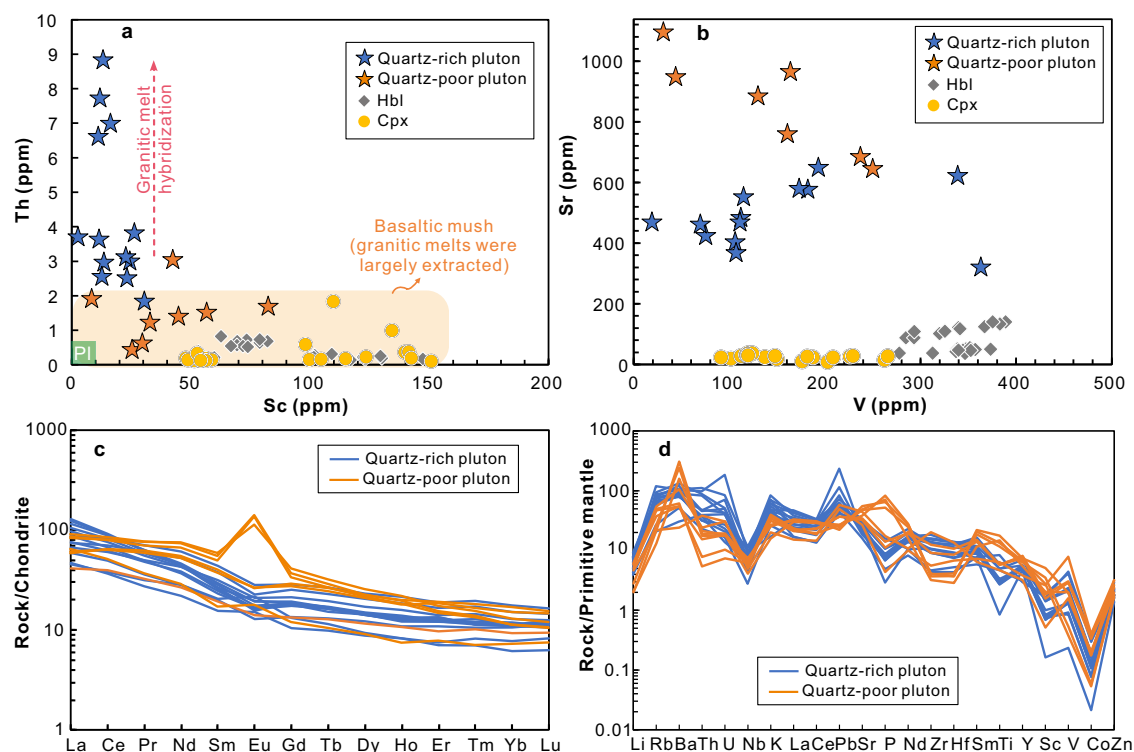
Fig. 5 | Variation of whole-rock trace elements to distinguish quartz-rich pluton from quartz-poor pluton. a–d Measured compositions of hornblende and clinopyroxene are also shown. Normalized data of chondrite and primitive mantle in c and d are from Sun and McDonough[48] and McDonough and Sun[49], respectively.

The addition of external and evolved melts into the crystal mush would promote more replacement of clinopyroxene by hornblende, considering that magma residual melts would also contribute to the formation of peritectic hornblende. On the other hand, chemical exchange between reactive melts and crystal matrix would create new reacted melts in equilibrium with the hornblende. The Hbl-equilibrium melts were estimated to be granitic ($SiO_2 > 65$ wt%) based on calculation methods from Putirka[37], Zhang et al.[38], and Higgins et al.[32] (Supplementary Data 2). However, the equilibrium melts have different fates in the two pluton types.

In the case of the quartz-poor pluton, the equilibrium melts may have been largely extracted, leaving dominantly earlier-crystalized mineral assemblages with reaction-rind relics as we observed (Figs. 2 and 3b). This is also supported by their low bulk-rock Th (mainly <2 ppm) and K_2O (mainly <1 wt%) contents (Figs. 4f and 5a), as these elements tend to be compatible with the granitic melt phase. On the other hand, the crystal mush of quartz-poor pluton exhibits high degree of anisotropy due to strong preferred orientation of plagioclase crystals (e.g., alignment factor of 0.46; Fig. 1g). The noticeable anisotropy of the crystals would have facilitated melt connectivity and extraction of interstitial melts[39]. As a result of almost complete melt extraction, the geochemical compositions of the quartz-poor samples were primarily determined by residual reacted solid assemblage (i.e., mainly plagioclase, hornblende, and clinopyroxene). Of them, the formation of hornblende was thought to be associated with reactive melt-involved peritectic reaction with clinopyroxene at the late magmatic stage. The near complete replacement of clinopyroxene by amphibole as exemplified by 15PG-21-3 (Fig. 3c) indicates the reactive melt had been quite pervasive and was likely present in abundance (or over a long time period). The plagioclase might be less influenced by reactive melt, as the compositional zoning associated with peritectic reaction was less documented within plagioclase of the quartz-poor plutons. As reactive melt infiltration could elevate the ratio of Cpx-Hbl replacement, we could predict that the combined reactive melt infiltration and complete extraction of equilibrium melt would elevate the bulk-rock

concentrations of most elements, such as Al_2O_3, FeO, Na_2O, K_2O, Ba, V, Zr, rare earth elements, etc (Figs. 4 and 6f), leading to chemical enrichment of the cumulate. On the other hand, this process only reduces the bulk-rock concentrations of several elements, including SiO_2, CaO, and Li (Figs. 4 and 6f), and slightly affects the concentrations of MgO, Rb, Pb, Hf, Th, and U (Figs. 4 and 6f). Different Cpx-Hbl replacement ratios would result in various bulk-rock compositions, while these ratios are determined by the extent of melt-crystal exchange. The input of Nd into the system through peritectic reaction potentially contributed to the enriched bulk Nd isotopes [ε_{Nd}(t) ranges from –3.8 to –2.7]. More importantly, both of the Cpx-Hbl replacement and the extraction of granitic equilibrium melt behaved in quartz-poor pluton would lead to a depletion of silica, giving rise to more mafic plutons ($SiO_2 = 43$–51 wt%) within crustal magmatic reservoirs (Figs. 4 and 8).

For the quartz-rich samples (Fig. 8b), they generally show weak mineral orientation (Fig. 1h) which declines the anisotropic distribution of interstitial melts and hinders the melt migration, making them a more optimal place for melt stalling relative to the quartz-poor samples. The equilibrium melts retained within quartz-rich samples might mainly present in interstitial quartz pseudomorph according to textural relations (Fig. 1), and partly have crystallized to albite rims on the pre-existing plagioclase grains (typically seen in sample 15PG-13-3; Supplementary Fig. 1) and interstitial mica. Therefore, the geochemistry of quartz-rich plutons may reflect variable hybridization of granitic equilibrium melts with reacted solid assemblage. Typical granitic melts are high in silica contents ($SiO_2 > 65$ wt%) and enriched in highly incompatible elements as illustrated in Chappell and White[40] (K_2O = ~4 wt%, Pb = ~20 ppm, La = ~30 ppm, Th = ~20 ppm, U = ~5 ppm, etc). Therefore, the elevated and various concentrations of SiO_2, Th, La, K_2O, and Pb in quartz-rich samples were mainly controlled by variable mixing of granitic melts (Figs. 4f and 5a). Mixing of granitic melts with mafic crystal frameworks would lead to further bulk-rock fertilization and could also be a dominant mechanism in the generation of the intermediate plutonic rocks (quartz-rich plutons: $SiO_2 = 50$–68 wt%) (Figs. 4 and 8).
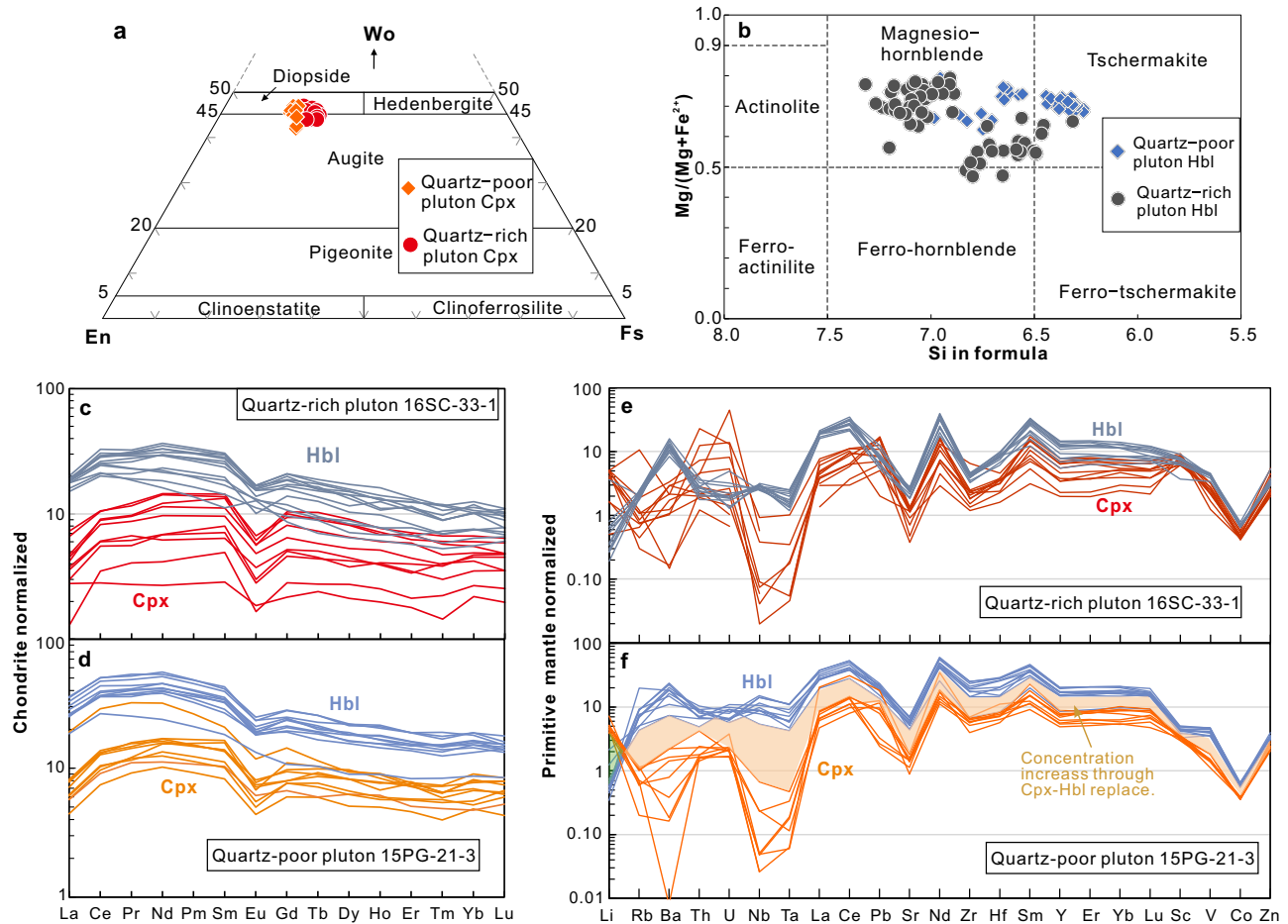
Fig. 6 | Mineral geochemistry of the studied samples. a, **b** Clinopyroxene (**a**) and hornblende (**b**) classification diagrams. **c–f** REE patterns (normalized to chondrite) (**c**, **d**) and trace element spidergrams (normalized to primitive mantle) (**e–f**) of clinopyroxene and hornblende from representative quartz-poor and quartz-rich samples. Normalized data of chondrite and primitive mantle are from Sun and McDonough[48] and McDonough and Sun[49], respectively. The light orange and green regions in Fig. **f** denote chemical enrichment and depletion induced by the Cpx-Hbl replacement respectively, as exemplified by the quartz-poor pluton 15PG-21-3.

Overall, our findings suggest that the basaltic mushy reservoirs in continental arc settings may evolve in an open and dynamic scenario and that the reactive melt infiltration is critical for differentiation of the mushy system (Fig. 8). First, the reactive melt can incorporate fertile crustal signatures into the basaltic mush system (Fig. 8a), resulting in mineral phase transformation and consequent change of bulk-rock geochemistry (including H_2O, major and trace elements, radiogenic and stable isotopes) (Figs. 4–7). Second, the interstitial, reacted, equilibrium granitic melts could be either extracted from or stored in crystal mush, which would further complicate the geochemistry of mushy systems and potentially make a compositional stratification of them (i.e., mafic and intermediate plutons at different crustal regions) (Fig. 8b, c). Our study lends further support for that the coupled melt migration and chemical exchange induced by reactive melt flow can be a dominant mechanism for chemical differentiation of basaltic mush reservoirs.

Methods
Mineral mapping
The mineral mapping of the studied samples was conducted at Nanjing Hongchuang Geological Exploration Technology Service Co., Ltd., using a TIMA (Tescan Integrated Mineral Analyzer) system which comprises a Mira-3 scanning electron microscope equipped with energy dispersive X-ray spectrometers (EDS, EDAX Element 30). The measurements were done with a dot mapping mode which includes the collection of BSE (Back-scattered Electron) and EDS

(Energy Dispersive X-ray Spectroscopy) data on a regular grid (9 μm dot spacing). The analyses were performed at 25 kV using a spot size of ~90 nm, and a working distance of 15 mm.

Mineral composition
Major element contents and BSE imaging of plagioclase, amphibole, pyroxene grains were conducted using a JXA-8230 (JEOL) electron microprobe analyzer (EMPA) at the Shandong Analysis Center of China Metallurgy Geology Bureau, Ji'nan, China. Operating conditions included a 15 kV accelerating voltage and a 20 nA beam current. A beam size of 10 μm at spot mode was applied. The analytical precision (i.e., one standard deviation) for major elements with mass proportions of >1 wt% is generally better than 2% (Supplementary Data 2). The EMPA data can accurately classify mineral type. These data were integrated into the TIMA images to obtain the updated images as shown in Fig. 3a, b. The trace element concentrations of minerals were determined by laser ablation inductively coupled plasma mass spectrometry (LA-ICP-MS) at the State Key Laboratory for Mineral Deposits Research, Nanjing University (MiDeR-NJU). The ablation was achieved with a GeoLas Pro 193 nm ablation system connected to a Thermal iCAP RQ ICP-MS. The repetition rate of the laser was set to 5 Hz with an energy density of ~7.5 J/cm^2 and a spot size of 32 μm. A single measurement lasted 60 s including 20 s background measurements. The NIST 610 reference material serves as an external standard and internal standardization to ^{29}Si. Laser-ablation spots were put on top of EMPA pits as much as possible and
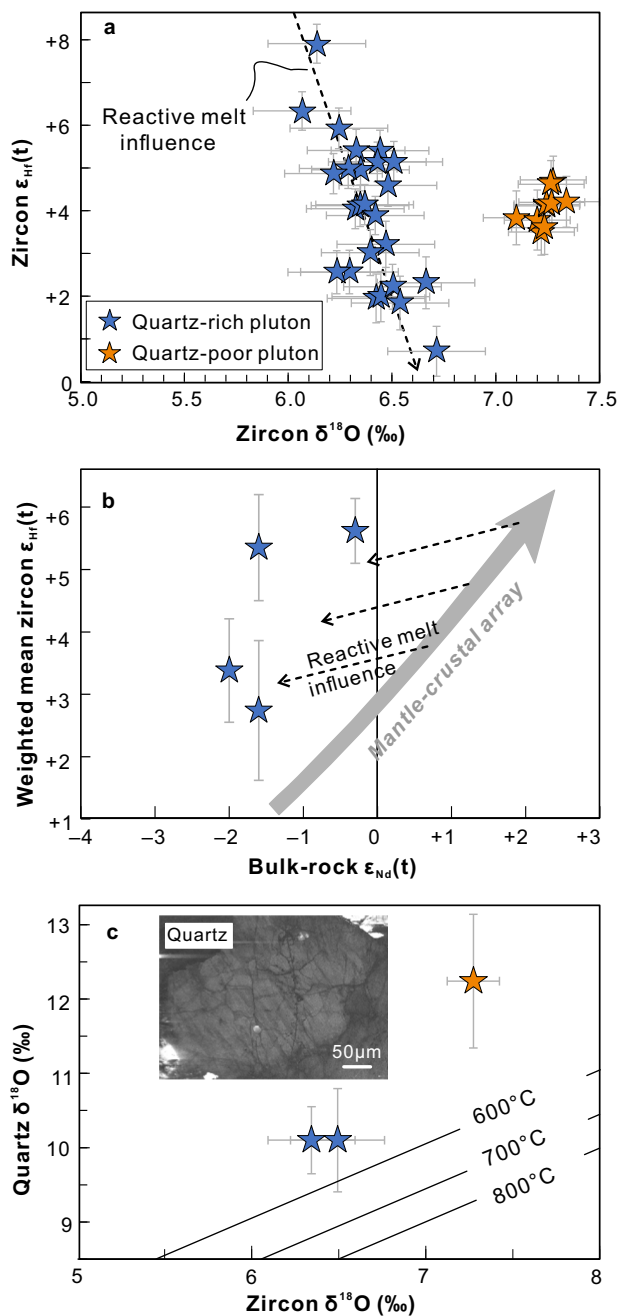
Fig. 7 | Diagrams showing the Hf, O, and Nd isotopic signatures that indicate the possible involvement of externally-derived reactive melts during magmatic differentiation. Error bars are shown at two standard errors. **a** Zircon $\varepsilon_{Hf}(t)$ vs. $\delta^{18}O$ diagram. **b** Correlation between weighted mean zircon $\varepsilon_{Hf}(t)$ values and bulk-rock $\varepsilon_{Nd}(t)$ values showing a considerable decoupling between them. **c** Quartz $\delta^{18}O$ vs. zircon $\delta^{18}O$ diagram showing a clear oxygen isotopic disequilibrium between quartz and zircon at magmatic temperatures. The representative quartz CL image is shown on the top left. Solid lines are calculated isotherms from the formula of Trail et al. [50].

hence Si contents obtained by EMPA could be used for normalization. The NIST 612 was used to monitor precision and accuracy, and the two standard deviations were generally with the range of ± 2.0–6.5 ppm for elements of interest (Supplementary Data 2). The concentration difference between measured and preferred values for most elements of NIST 612 is within ±6 ppm (Supplementary Data 2). The LA-ICP-MS raw data were reduced using the GLITTER

4.4 software[41]. The 1σ error was based on counting statistics from signal.

Whole-rock composition
Whole-rock major elements for the samples were analyzed using a Thermal Scientific ARL 9900 X-ray fluorescence spectrometer (XRF) at MiDeR-NJU, following the method similar to Franzini et al.[42] SY-4, SARM-45, SCH-1, SARM-43, GBW07103, GBW07104, and GBW07105 standards were used for quality control. The analytical precision (RSD) is 1–3% for elements with contents above 1 wt% and is better than 6 % for elements with contents below 1 wt%. For whole-rock trace elements, about 50 mg of sample powder for each sample was digested using a mixture of concentrated $HF + HNO_3$ in Teflon bombs. Then, trace element concentrations of dissolved samples were determined by an Agilent 7700x inductively coupled plasma-mass spectrometer (ICP-MS) at Nanjing FocuMS Technology Co. Ltd. Following the procedures of Gao et al.[43] AGV-1, W-2, BHVO-2, RGM-2, GSP-2, AMH-1, GBPG-1, and OU-6 standards were used to monitor the instrument performance. The analytical precisions are generally better than 5%. Whole-rock Rb–Sr and Sm–Nd isotopic compositions were measured using a Finnigan Triton TI thermal ionization mass spectrometer (TIMS) and the Neptune (Plus) MC-ICP-MS respectively at MiDeR-NJU, following the methods of Pu et al.[44,45]. The detailed analytical procedures and parameters for the calculations of $(^{87}Sr/^{86}Sr)_i$, $\varepsilon_{Nd}(t)$ and Nd model ages are shown in supplementary Data 1.

Zircon isotopes
Zircon grains were separated using conventional density and magnetic techniques, mounted in epoxy resin disk, and polished to expose their internal texture. The structures in zircon were then studied using CL imaging. Three samples were chosen for zircon U-Pb-O isotope analyses using Cameca IMS-1300HR³ SIMS at the MiDeR-NJU, while seven samples were chosen for zircon U-Pb dating using LA-ICP-MS at MiDeR-NJU. Zircon Lu-Hf isotopic analyses were conducted using a GeoLas 193 nm laser-ablation system attached to a Neptune (Plus) MC-ICP-MS at MiDeR-NJU. The detailed analytical procedures for above isotopes are followed Li et al.[29].

Quartz O isotopes
We first cut the hand samples to millimeter to centimeter-sized rock chips and embedded the chips near the center of 1 inch diameter epoxy plugs. After curing the epoxy mount two days at 50 ℃, the samples were first grounded by sand papers, and then polished by 3 μm and 1 μm diamond polishing liquids respectively. After a flat surface was obtained, small (~1 mm) holes were drilled within 5 mm of the sample center to accommodate a quartz standard (UWQ-1; Kelley et al.[46]). The holes were filled with epoxy and after curing at ~50 ℃ for two days, the resulting epoxy protuberances were brought to level with the sample with 1 μm diamond polishing liquid. The Quartz O-isotope analyses were performed with a CAMECA IMS-1300HR at MiDeR-NJU. Sampling spots were selected based on detailed SEM and reflected images. All analysis spots were selected within a radius of 5 mm from the center of the mount. A ~ 2–3 nA primary Cs^+ beam focused to a spot size of ~10 × 15 μm was applied to the analysis. Secondary ions of $^{16}O^-$ and $^{18}O^-$ were detected simultaneously with two faraday cup detectors, L2' ($10^{10}\Omega$) and H2' ($10^{11}\Omega$), respectively. Counting rates for ^{16}O were ~1.4–2.3 × 10⁹ cps. Mass resolving power was 2400 at 50% peak height. The UWQ-1 quartz standard was analyzed once every three unknown quartz samples, with two analyses of UWQ-1 quartz standards made before and after each group of analyses. The spot-to-spot reproducibility of each group of 8 standard analyses averages ±0.13‰, ±0.22‰ and ±0.32‰ (2 SD), respectively, and the standard errors are ±0.10–0.19 ‰ (2SE).
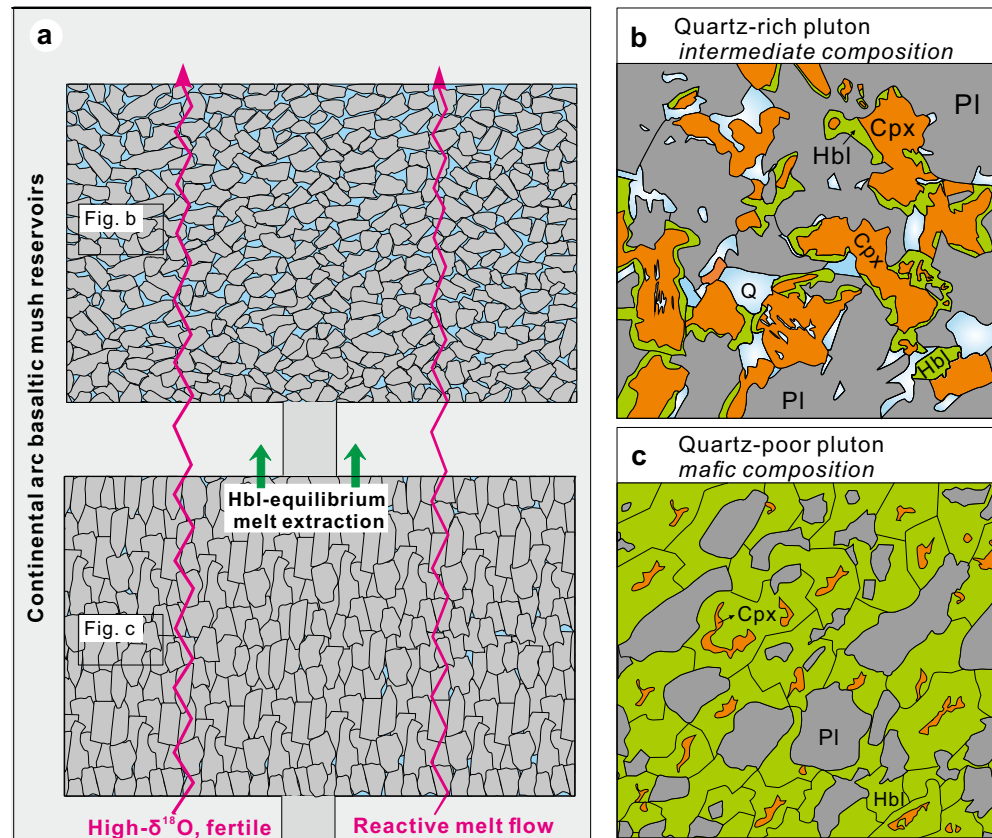
Fig. 8 | A conceptual model illustrating an upper crustal basaltic mush reservoir modulated by the reactive melt flow under continental arc setting. a A simplified cartoon model showing the fertile reactive melt flow ascended through and reacted with the crystal mush at different regions of upper continental crust in this study. The Hbl-equilibrium melt was prone to either stall in the crystal mush (**b**) or be efficiently extracted from the crystal mush (**c**). **b**, **c** Simplified micrographic mineral and chemical relations of intermediate quartz-rich and mafic quartz-poor crystal mushes.

Data availability

The dataset that supports the findings of this study is available in Supplementary Information and Supplementary Data 1–5. In addition, these supplementary files can be found in the online open-access repository at https://doi.org/10.6084/m9.figshare.25045631.

References

1. Cashman, K. V., Sparks, R. S. J. & Blundy, J. D. Vertically extensive and unstable magmatic systems: a unified view of igneous processes. *Science* **355**, eaag3055 (2017).
2. Edmonds, M., Cashman, K. V., Holness, M. & Jackson, M. Architecture and dynamics of magma reservoirs. *Phil. Trans. R. Soc. A* **377**, 20180298 (2019).
3. Lissenberg, C. J., MacLeod, C. J. & Bennett, E. N. Consequences of a crystal mush-dominated magma plumbing system: a mid-ocean ridge perspective. *Phil. Trans. R. Soc. A* **377**, 20180014 (2019).
4. Sparks, R. S. J. et al. Formation and dynamics of magma reservoirs. *Phil. Trans. R. Soc. A* **377**, 20180019 (2019).
5. Brown, G. M. The layered ultrabasic rocks of Rhum, Inner Hebrides. *Phil. Trans. R. Soc. Lond.* **240**, 1–53 (1956).
6. Huppert, H. & Sparks, R. S. J. The fluid dynamics of a basaltic magma chamber replenished by influx of hot, dense ultrabasic magma. *Contrib. Mineral. Petrol.* **75**, 279–289 (1980).
7. Bachmann, O. & Bergantz, G. W. On the origin of crystal-poor rhyolites: extracted from batholithic crystal mushes. *J. Petrol.* **45**, 1565–1582 (2004).
8. Hildreth, W. Volcanological perspectives on Long Valley, Mammoth Mountain, and Mono Craters: several contiguous but discrete systems. *J. Volcanol. Geotherm. Res.* **136**, 169–198 (2004).
9. McKenzie, D. Compaction and crystallization in magma chambers: towards a model of the Skaergaard Intrusion. *J. Petrol.* **52**, 905–930 (2011).
10. Schmidt, M. W., Forien, M., Solferino, G. & Bagdassarov, N. Settling and compaction of olivine in basaltic magmas: an experimental study on the time scales of cumulate formation. *Contrib. Mineral. Petrol.* **164**, 959–976 (2012).
11. Holness, M. B., Vukmanovic, Z. & Mariana, E. Assessing the role of compaction in the formation of adcumulates: a microstructural perspective. *J. Petrol.* **58**, 643–674 (2017).
12. Leuthold, J., Blundy, J. D., Holness, M. B. & Sides, R. Successive episodes of reactive liquid flow through a layered intrusion (Unit 9, Rum Eastern Layered Intrusion, Scotland). *Contrib. Mineral. Petrol.* **168**, 1021 (2014).
13. Solano, J., Jackson, M. D., Sparks, R. S. J. & Blundy, J. D. Evolution of major and trace element composition during melt migration through crystalline mush: implications for chemical differentiation in the crust. *Am. J. Sci.* **314**, 895–939 (2014).
14. Cooper, G. F., Davidson, J. P. & Blundy, J. D. Plutonic xenoliths from Martinique, Lesser Antilles: evidence for open system processes and reactive melt flow in island arc crust. *Contrib. Mineral. Petrol.* **171**, 87 (2016).
15. Lissenberg, C. J. & MacLeod, C. J. A reactive porous flow control on mid-ocean ridge magmatic evolution. *J. Petrol.* **57**, 2195–2220 (2016).
16. Jackson, M., Blundy, J. & Sparks, R. S. J. Chemical differentiation, cold storage and remobilization of magma in the Earth's crust. *Nature* **355**, eaag3055 (2018).

17. Gleeson, M. L. M., Lissenberg, C. J. & Antoshechkina, P. M. Porosity evolution of mafic crystal mush during reactive flow. *Nat. Commun.* **14**, 3088 (2023).

18. Mathez, E. A. Magmatic metasomatism and formation of the Merensky reef, Bushveld Complex. *Contrib. Mineral. Petrol.* **119**, 277–286 (1995).

19. Holness, M. B., Hallworth, M. A., Woods, A. & Sides, R. E. Infiltration metasomatism of cumulates by intrusive magma replenishment: the Wavy Horizon, Isle of Rum, Scotland. *J. Petrol.* **48**, 563–587 (2007).

20. Namur, O., Humphreys, M. C. & Holness, M. B. Lateral reactive infiltration in a vertical gabbroic crystal mush, Skaergaard intrusion, East Greenland. *J. Petrol.* **54**, 985–1016 (2013).

21. Gao, Y., Hoefs, J., Hellebrand, E., von der Handt, A. & Snow, J. E. Trace element zoning in pyroxenes from ODP Hole 735B gabbros: diffusive exchange or synkinematic crystal fractionation? *Contrib. Mineral. Petrol.* **153**, 429–442 (2007).

22. Boulanger, M. et al. Magma reservoir formation and evolution at a slow-spreading center (Atlantis Bank, Southwest Indian Ridge). *Front. Earth Sci.* **8**, 554598 (2020).

23. Gleeson, M. L. M., Gibson, S. A. & Stock, M. J. Upper mantle mush zones beneath low melt flux ocean island volcanoes: insights from Isla Floreana, Galápagos. *J. Petrol.* **61**, egaa094 (2020).

24. Ducea, M. N., Saleeby, J. B. & Bergantz, G. The architecture, chemistry, and evolution of continental magmatic arcs. *Ann. Rev. Earth Planet. Sci.* **43**, 299–331 (2015).

25. Zhou, M. F., Yan, D. P., Kennedy, A. K., Li, Y. & Ding, J. SHRIMP U–Pb zircon geochronological and geochemical evidence for Neoproterozoic arc-magmatism along the western margin of the Yangtze Block, South China. *Earth Planet. Sci. Lett.* **196**, 51–67 (2002).

26. Zhao, J. H., Li, Q. W., Liu, H. & Wang, W. Neoproterozoic magmatism in the western and northern margins of the Yangtze Block (South China) controlled by slab subduction and subduction-transform-edge-propagator. *Earth-Sci. Rev.* **187**, 1–18 (2018).

27. Zhu, Y. et al. Petrogenesis and geodynamic implications of Neoproterozoic gabbro-diorites, adakitic granites, and A-type granites in the southwestern margin of the Yangtze Block, South China. *J. Asian Earth Sci.* **193**, 103977 (2019).

28. Wang, E. C. & Meng, Q. R. Mesozoic and Cenozoic tectonic evolution of the Longmenshan fault belt. *Sci. China Ser. D-Earth Sci.* **52**, 579–592 (2009).

29. Li, J. Y. et al. Rapid endogenic rock recycling in magmatic arcs. *Nat.e Comm.* **12**, 3533 (2021).

30. Smith, D. J. Clinopyroxene precursors to amphibole sponge in arc crust. *Nat. Commun.* **5**, 4329 (2014).

31. Rusk, B. *Quartz: Deposits, mineralogy and analytics* (eds. Götze, J., Möckel, R.) p. 307–329 (Springer, 2012).

32. Higgins, O., Sheldrake, T. & Caricchi, L. Machine learning thermobarometry and chemometry using amphibole and clinopyroxene: a window into the roots of an arc volcano (Mount Liamuiga, Saint Kitts). *Contrib. Mineral. Petrol.* **177**, 10 (2022).

33. Liao, Y., Wei, C. & Rehman, H. U. Titanium in calcium amphibole: Behavior and thermometry. *Am. Mineral.* **106**, 180–191 (2021).

34. Lee, C. T. A. & Bachmann, O. How important is the role of crystal fractionation in making intermediate magmas? Insights from Zr and P systematics. *Earth Planet. Sci. Lett.* **393**, 266–274 (2014).

35. King, M., Barrie, C. T. & Valley, J. W. Hydrothermal alteration of oxygen isotope ratios in quartz phenocrysts, Kidd Creek mine, Ontario: magmatic values are preserved in zircon. *Geology* **25**, 1079–1082 (1997).

36. Rosenberg, C. L. & Handy, M. R. Experimental deformation of partially melted granite revisited: implications for the continental crust. *J. Metamorph. Geol.* **23**, 19–28 (2005).

37. Putirka, K. Amphibole thermometers and barometers for igneous systems and some implications for eruption mechanisms of felsic magmas at arc volcanoes. *Am. Mineral.* **101**, 841–858 (2016).

38. Zhang, J., Humphreys, M. C. S., Cooper, G. F., Davidson, J. P. & Macpherson, C. G. Magma mush chemistry at subduction zones, revealed by new melt major element inversion from calcic amphiboles. *Am. Mineral.* **102**, 1353–1367 (2017).

39. Liu, B. D. & Lee, C. T. A. Fast melt expulsion from crystal-rich mushes via induced anisotropic permeability. *Earth Plant. Sci. Lett.* **571**, 11711 (2021).

40. Chappell, B. W. & White, A. J. R. I- and S-type granites in the Lachlan fold belt. *Trans. R. Soc. Edinburgh Earth Sci.* **83**, 1–26 (1992).

41. Griffin, W. L., Powell, W. J., Pearson, N. J. & O'Reilly, S. Y. *Laser Ablation-ICP-MS in the Earth Sciences* (ed. Sylvester, P.). Vol. 40, p. 204–207 (2008).

42. Franzini, M., Leoni, L. & Saitta, M. A simple method to evaluate the matrix effects in X-ray fluorescence analysis. *X-Ray Spectrum.* **1**, 151–154 (1972).

43. Gao, J. F., Lu, J. J., Lai, M. Y., Lin, Y. P. & Wu, P. Analysis of trace elements in rock samples using HR-ICP-MS. *J. Nanjing Univer. (Nat. Sci.)* **39**, 844–850 (2003).

44. Pu, W., Gao, J. F., Zhao, K. D., Ling, H. F. & Jiang, S. Y. Separation method of Rb–Sr, Sm–Nd using DCTA and HIBA. *J. Nanjing Univer. (Nat. Sci.)* **41**, 445–450 (2005).

45. Pu, W., Zhao, K. D., Ling, H. F. & Jiang, S. Y. High precision Nd isotope measurement by Triton TI Mass Spectrometry. *Acta Geosci. Sin.* **25**, 271–274 (2004).

46. Kelly, J. L., Fu, B., Kita, N. T. & Valley, J. W. Optically continuous silcrete quartz cements of the St. Peter Sandstone: high precision oxygen isotope analysis by ion microprobe. *Geochim. Cosmochim. Acta* **71**, 3812–3832 (2007).

47. Higgins, M. D. *Quantitative Textural Measurements in Igneous and Metamorphic Petrology*, p. 276 (Cambridge University Press, 2006).

48. Sun, S. & McDonough, W. Chemical and isotopic systematics of oceanic basalts: implications for mantle composition and processes. *Geol. Soc. Lond. Spec. Pub.* **42**, 313–345 (1989).

49. McDonough, W. & Sun, S. The composition of the Earth. *Chem. Geol.* **120**, 223–253 (1995).

50. Trail, D., Bindeman, I. N., Watson, E. B. & Schmitt, A. K. Experimental calibration of oxygen isotope fractionation between quartz and zircon. *Geochim. Cosmochim. Acta* **73**, 7110–7126 (2009).

Acknowledgements

Author contributions

J.Y.Li, X.L.Wang, and Z.D.Gu designed the study and prepared the manuscript with the help of D.Wang and D.H.Du. All co-authors contributed to the interpretation presented in the manuscript.

Competing interests

The authors declare no competing interests.

Additional information

Supplementary information The online version contains supplementary material available at https://doi.org/10.1038/s43247-024-01279-w.

Correspondence and requests for materials should be addressed to Xiao-Lei Wang.

Peer review information *Communications Earth & Environment* thanks Qiang Wang and the other, anonymous, reviewer(s) for their contribution to the peer review of this work. Primary Handling Editor: Joe Aslin. A peer review file is available.

Reprints and permissions information is available at http://www.nature.com/reprints

Publisher's note Springer Nature remains neutral with regard to jurisdictional claims in published maps and institutional affiliations.